Journal of Applied Mathematics and Physics, 2022, 10, 1587-1601
https://www.scirp.org/journal/jamp
ISSN Online: 2327-4379
ISSN Print: 2327-4352

Quantitative Simulation Study of Metal Additive Manufacturing by Kinetic Monte Carlo

Kepeng Ouyang[1], Youdi Kuang[1,2*]

[1]School of Mechanics and Construction Engineering, MOE Key Laboratory of Disaster Forecast and Control in Engineering, Jinan University, Guangzhou, China
[2]School of Civil Engineering and Architecture, Wuyi University, Jiangmen, China
Email: *kuangzhang88@gmail.com

How to cite this paper: Ouyang, K.P. and Kuang, Y.D. (2022) Quantitative Simulation Study of Metal Additive Manufacturing by Kinetic Monte Carlo. *Journal of Applied Mathematics and Physics*, **10**, 1587-1601.
https://doi.org/10.4236/jamp.2022.105110

Received: April 18, 2022
Accepted: May 15, 2022
Published: May 18, 2022

Abstract

Metal additive manufacturing (AM) is a disruptive manufacturing technology that takes into account the needs of complex structural forming and high-performance component forming. At present, the understanding of metal additive manufacturing simulation methods is not thorough enough, which restricts the development of metal additive manufacturing. Present work discusses the evolution of KMC method simulation results for simulating metal additive manufacturing at different length ratios and different scanning speeds. The results reveal that as the scanning speed increases, the main grains in the simulation results are transformed from coarse columnar grains to crescent-shaped grains, which are in good agreement with the existing experimental results. Besides, as the ratio of unit physical length to unit simulation length increases, the ratio of unit physical time to unit simulation time gradually decreases.

Keywords

Additive Manufacturing, Kinetic Monte Carlo Simulation, Grain Morphology

1. Introduction

Metal additive manufacturing (AM) is a disruptive manufacturing technology that takes into account the needs of complex structural forming and high-performance component forming. Traction is gaining in industrial manufacturing for additive manufacturing, which is widely used in various industrial fields like consumer products, automotive, health care, energy, aerospace. From 2014 to 2019, the number of new patents filed for metal additive manufacturing has surpassed casting and forging. The sales of additive manufacturing equipment are also

growing rapidly, and the sales of additive manufacturing printers in 2017 are 5 times more than those in 2013 [1].

Under this circumstance, the development and engineering application of metal additive manufacturing technology still faces many difficulties and challenges. For example, understanding of metal additive manufacturing simulation methods is not incisive enough. According to ASTM standard F2792, there are two main processes for metal additive manufacturing: powder bed fusion (PBF) and directed energy deposition (DED) [2]. The DED process constructs products by depositing material layer by layer through feeding powder directly into a set heat source path or meltpool. The PBF process constructs products layer by layer through melting the paved powder material according to the set heat source movement path. Substantially, no matter which kind of process is applied, the essence of metal additive manufacturing is the process of melting and rapidly solidifying metal materials through a heat source based on a set path [3]. In the process of additive manufacturing, there is a complex temperature field and flow field. These fields would eventually make the product presenting a unique microstructure, which is different from casting and forging processes.

In additive manufacturing process, the microstructure of various metals can be experimental. For example, using EBSD, An *et al.* [4] observed the microstructure of IN625 curved thin-walled structures fabricated, which are processed by additive manufacturing. Nagase *et al.* [5] used EBSD to explore the microstructure of Ti-based alloys. Ishimoto *et al.* [6] explored the evolution law of the microstructure of 316L steel under the scanning strategy of parallel scanning by EBSD. So, experiment is obviously a direct method to study metal additive manufacturing. However, it is also highly costly and time-consuming, and when it comes to some complex processes, experiments are difficult to be conducted. Therefore, bringing up simulation method is necessary.

At present, there are three main simulation methods for simulating the microstructure of metal additive manufacturing: the Phase Field (PF) method, the Cellular Automata (CA) method, and the Kinetic Monte Carlo (KMC) method. They each have their own features. The PF method can simulate the dendrite structure well, but the calculations need a great amount of efforts [7] [8] [9]. The CA model is suitable for simulating the grain structure, but it has many a priori parameters and calculations are still demanding when dealing with multiple layers and multiple scanning paths [7] [8] [10]. In comparison, KMC only needs small amount of calculation for the models, which means that this model is very suitable for large-scale simulations with multiple layers and multiple scanning paths [11] [12] [13]. That's why it is chosen in this study.

One of the challenges in using the KMC method is how to match the simulated input parameters with the experimental parameters. Rodgers *et al.* provide a qualitative approach to aid in fitting simulated input parameters to experimental parameters [12]. However, this method does not provide quantitative examples for reference, and does not study the effect of the actual unit physical

length ratio to unit simulation length on the simulation results. Such problem makes it difficult to simulate additive manufacturing when using the KMC method.

In order to solve the above-mentioned challenges of KMC application, this work carried out KMC simulations with five different speeds and three different length ratios as input parameters, discussed the evolution law in the simulation results and explored the effect of length ratio on the simulation results.

2. Simulation Method

2.1. Kinetic Monte Carlo (KMC) Model

The Kinetic Monte Carlo (KMC) Model is completely probabilistic simulation model [7], which simulates the progress of additive manufacturing by random sampling. It is based on Potts model.

Potts model is introduced below. At the beginning of the simulation, a discrete lattice is set to describe the simulation area. All the lattice sites have their value called "spin". Grains in the simulation area are made up of lattice sites with the same "spin". Total energy of the system connects with "spin", and every lattice site has neighbors. If the lattice site has spin different from its neighbor, the total energy of the system would be added. On the other hand, if the lattice site has "spin" the same with its neighbor, the total energy of the system would remain the same. All lattice sites have possibility to change its spin to its neighbors' spin, which would lead the change of the total energy of the system. The probability of change acceptance, P, follows Equation (1) [11] [12] [13]:

$$P = \begin{cases} \exp\left(\dfrac{-\Delta E}{K_b T_s}\right) & \Delta E > 0 \\ 1 & \Delta E \le 0 \end{cases} \tag{1}$$

K_b is Boltzmann constant and T_s is the simulation background temperature. In fact, T_s is not a real temperature in the simulation. $K_b T_s$ stands for a parameter that represents energy fluctuations [14]. If the system receives significant interference, the $K_b T_s$ will be set to a higher value. ΔE is the total energy difference. Total energy of the system follows Equation (2) [11] [12] [13]:

$$E = \frac{1}{2}\sum_{i=1}^{N}\sum_{j=1}^{L}\left[1-\delta\left(q_i, q_j\right)\right] \tag{2}$$

q_i is the spin of each lattice site in the system. q_j is the spin of each neighbor lattice site. N is the number of lattice sites in the system and L is the number of neighbors. Monte Carlo Step (MCS) is used to represent the simulation time. Every MCS pass, all the lattice sites in the system are updated.

Potts model is modified to simulate the metal additive manufacturing by Rodgers *et al.* [12]. A heat-affected zone (HAZ) is set, which surrounds the molten pool. Only the lattice sites within the HAZ would change their spin. This is reasonable because grain growth doesn't take place when it is far from the melt-pool. And a grain boundary mobility, M, follows the Equation (3):

$$M(T) = M_0 \exp\left(\frac{-Q}{RT}\right) \tag{3}$$

Q is activation energy for grain boundary motion. R is the gas constant and T is the local temperature near the meltpool. M_0 is the Arrhenius pre-factor. Substituting Equation (3) into Equation (1), the probability of change acceptance, P, follows Equation (4):

$$P = \begin{cases} M(T)\exp\left(\dfrac{-\Delta E}{K_b T_s}\right) & \Delta E > 0 \\ M(T) & \Delta E \le 0 \end{cases} \tag{4}$$

It is worth mentioning that T and T_s are not a same parameter. T is a real physical temperature. $K_b T_s$ can be set to 0 without severe error, and in this study, it is also set to 0 [14]. Equation (4) shows that the higher the temperature of the lattice site is, the higher the probability that the change will be accepted, and if the temperature is trending low, the change will be less possible to be accepted.

In practical simulation applications, $M(T)$ is often replaced by $M(d)$ because it is a variable associated with the lattice site position. $M(d)$ is not unique and has many forms, depending on the temperature field model. In the open-source KMC software, SPPARKS, $M(d)$ follows Equation (5):

$$M(d) = \exp(-exp\_factor \cdot d) \tag{5}$$

exp_factor is user-defined parameter, which reflects the influence of temperature gradient, and d represents the shortest distance from the lattice site to the meltpool boundary. The closer the lattice site is to the meltpool, the higher the possibility of accepting would change. The grain boundary mobility for this work will all be calculated using Equation (5).

2.2. Details of Simulation

To explore the effect of different simulation length ratios and simulation speeds within the simulation, three groups of simulation at different length ratios are carried out. The length ratio is the ratio of unit physical length to unit simulation length. For each length ratio, there are 5 simulations, all of which have different scanning speeds.

The scanning strategy is shown in **Figure 1**. A parallel scanning strategy is adopted, which means that the rotation angle between layers is 0 degrees. The advantage of using the parallel scanning strategy in the simulation is that the properties of the entire simulation result can be comprehended through the BD-TD plane, which is convenient for observation during simulation and experiment. Therefore, it is easier to match the simulation results with the experimental results in practical use, and laying a foundation for the simulation of other scanning strategies.

Each simulation has 6 layers with 5 scanning paths per layer. The input parameters of the KMC model are shown in the table 1 below, including the geometric parameters of the meltpool and other parameters. Double ellipsoid model is

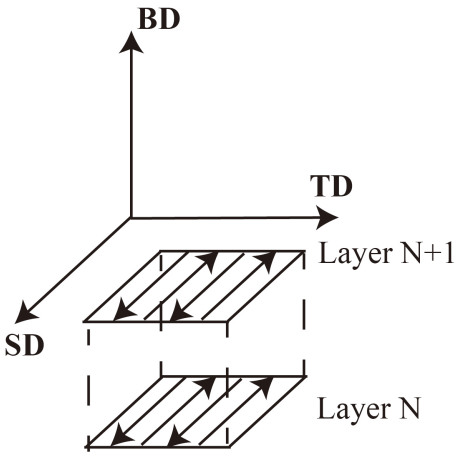

Figure 1. The scanning strategy of the simulation. The parallel scanning strategy is adopted, and the rotation angle between layers is 0 degrees.

applied to the meltpool, and the detailed definition of its geometric parameters and heat affected zone (meltpool width, tail length, depth, HAZ and cap height) can refer to the work of Rodgers [11] [13]. This study does not focus on a certain material or process. The geometric parameters are set to reflect the shape of the meltpool in a typical metal additive manufacturing process. When KMC is employed in actual production, the geometric parameters will be different based on different processes and materials, which are generally obtained by temperature field model simulation or experimental observation. In addition, Hatch in Table 1 represents the scanning pitch of two adjacent laser beams.

As the length ratio increases, lattice site of the simulation area turns denser and denser. It should be noticed that the input parameter changes proportionally as the ratio changes. Therefore, three groups with different length ratios simulate the same physical simulation domain and meltpool. Each group contains 5 sets of speed, which correspond to the same set of 5 physical speeds. The *exp_factor* also be put up different value to ensure that the $M(d)$ is the same when the physical length is the same at different length ratios.

3. Simulation Results and Discussion

3.1. Grain Morphologies of Simulation Results

In the simulation results of this study, the three coordinate axes are correspond to the Building Direction (BD); Scanning Direction (SD); Transverse Direction (TD). Perceiving BD-TD plane can acquire the microstructural properties of the entire simulation result, since the properties of the planes are similar along the Scanning Direction (SD). BD-SD plane reflects the grain morphology of the plane, where the scanning path is located. SD-TD plane shows the plane where the top of each layer of the meltpool is located. It presents the grain morphology between different paths within each layer. The coordinate system and scanning paths in the simulation results are shown in Figure 2(f), Figure 3(f), Figure 4(f).

Table 1. Input parameters of the simulation.

Parameter	Group A	Group B	Group C
Length Ratio (μm/site)	0.6	0.8	1.0
Meltpool width (site)	82	110	137
Meltpool tail length (site)	205	274	342
Meltpool depth (site)	41	54	68
HAZ width (site)	90	120	150
Cap length (site)	18	24	30
Speed (site/MCS)	10; 15; 20; 25; 30	13; 20; 27; 33; 40	17; 25; 33; 42; 50
Layer thickness (site)	24	32	40
Hatch (site)	66	88	110
exp_factor	0.1	0.075	0.06

Figure 2 reveals the simulation results of Group A with the length ratio equal to 0.6 (μm /site = 0.6). The morphologies of the grains are all inconsistent in the results of the 5 sets of scanning speeds.

In the BD-TD plane, coarse columnar grains throughout several layers appear in (a) and (b) of Figure 2. These coarse columnar grains penetrate to the top of the simulation area. If the simulations go on, they probably keep growing without being interrupted. As the speed increases, crescent-shaped grains appear in Figure 2(c) and Figure 2(d). Coarse columnar grain is still present in Figure 2(c) but is interrupted at the topmost layer of the simulation. At this scanning speed, columnar grains that grow uninterrupted are unlikely to emerge. In Figure 2(e), there are still crescent-shaped grains. Meanwhile, small strip-shaped columnar grains grow along the BD direction at the position where the scanning path passes. These strip-shaped columnar grains are arranged along the TD direction with the length of scanning hatch as the period, and 1-2 grains are arranged laterally in each period. They are also arranged with layer thickness as a period in the BD direction, and the length of each grain is about the length of one layer thickness.

In the BD-SD plane, as shown in Figure 2, the morphologies of the grains are all inconsistent in the results of the different scanning speeds as well. Strip-shaped grains running through several layers of layer thickness appear in Figure 2(a) and Figure 2(b). Those grains grow to the top of the simulation area, corresponding to the shape of coarse columnar grains observed in BD-TD plane in other direction. They are the dominant morphology of the grains. If the simulations proceed, they may also keep growing without interception. Many strip-shaped grains through two or three layers of thickness are observed in Figure 2(c) and Figure 2(d), corresponding to the transverse section of the crescent-shaped grains in the BD-TD plane. In Figure 2(e), many strip-shaped grains with a length of one layer thickness are arranged in the BD-SD plane. They reflect the transverse section of the strip-shaped grains in the BD-TD plane.

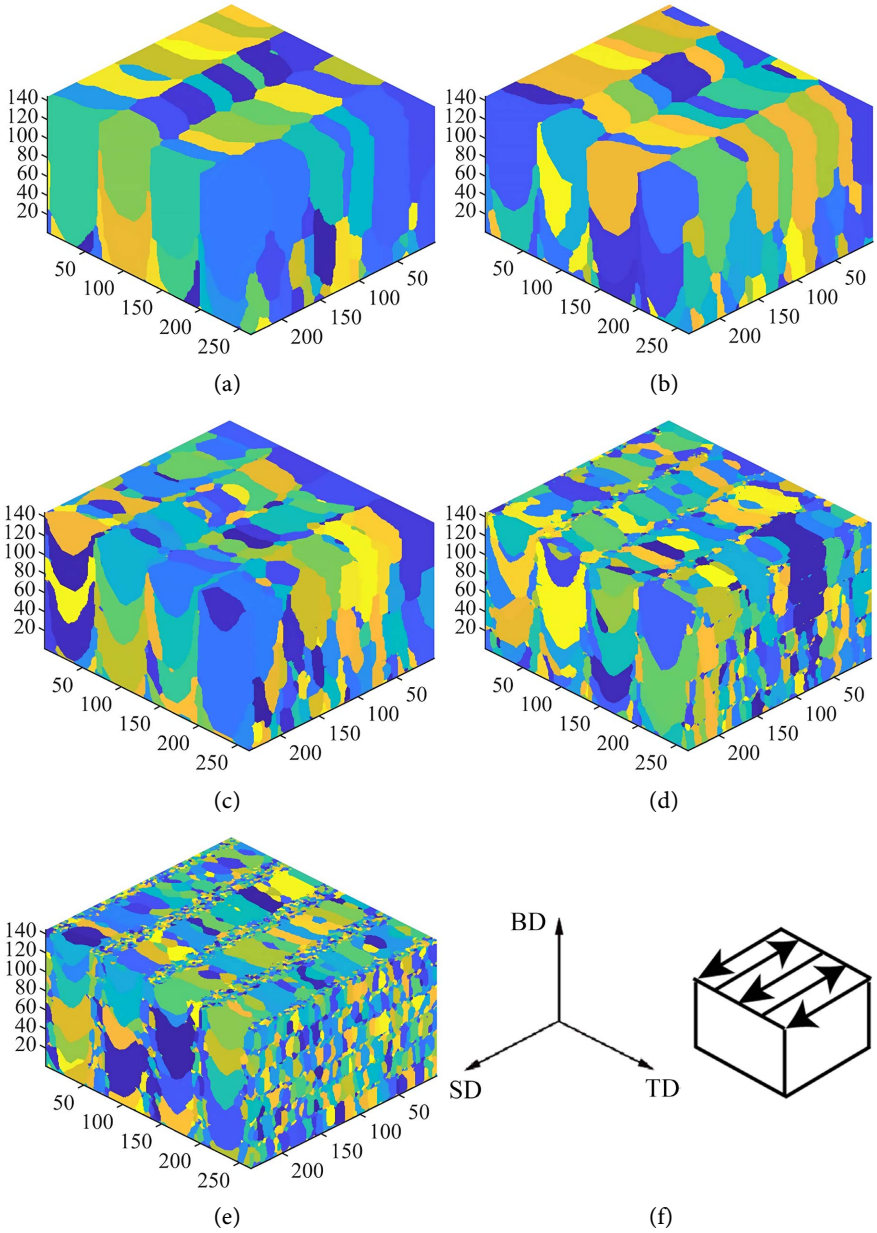

Figure 2. Simulation results of Group A. Five simulation results for five different scanning speeds, where (a) Speed = 10 site/MCS (b) Speed = 15 site/MCS (c) Speed = 20 site/MCS (d) Speed = 25 site/MCS (e) Speed = 30 site/MCS. (f) The coordinate system and scanning paths in the simulation results.

In the SD-TD plane, strip-shaped grains can be observed sandwiched between the two scanning paths. In Figure 2(a) and Figure 2(b), they are corresponding to the top section of the coarse columnar grains in the BD-TD plane. The length of the strip-shaped grains is nearly equal to the length of scanning hatch, and can be observed to be shorter in Figure 2(c) and Figure 2(d) than those in Figure 2(a) and Figure 2(b), since they are the top section of the crescent-shaped grains in BD-TD plane in Figure 2(c) and Figure 2(d). Several small round grains are observed at the scanning paths. They are the tips of the crescent-shaped

grains in the BD-TD section, which will be displayed as a circle from depression angle. As shown in **Figure 2(e)**, the strip-shaped grains become shorter and shorter with the increase of scanning speed. Raising in number of small round grains on the scanning paths can be observed, and these small round grains consist of the top section of the grains. They include crescent-shaped grain tips and strip-shaped grains observed in the BD-TD plane. In addition, there are also small equiaxed grains with a size of only about 1-2 lattice sites in the plane. These equiaxed grains exist in the scanning paths on top of each layer. It is worth mentioning that they are not easily observed in the BD-TD plane and the BD-SD plane, which is the reason why they are not brought up in other planes.

Figure 3 exhibits the simulation results of Group B with the length ratio equal to 0.8 (μm/site = 0.8). The grain morphologies of 5 sets of speed are also different as shown in **Figure 3**.

In the BD-TD plane, as shown in **Figure 3(a)**, grain morphology of the mixture of crescent-shaped grains and coarse columnar grains running through several layers is presented. The coarse columnar grains also grow to the top of the simulation area, which is the same with **Figure 2(a)**. If simulation continues, the original coarse columnar grains probably continue to grow, and the position of the crescent-shaped grains also potentially generates new crescent-shaped grains or new coarse columnar grains. In **Figure 3(b)**, there are also crescent-shaped grains and coarse columnar grains that run through several layers, but unlike **Figure 3(a)**, the dominant grains are crescent-shaped grains. So, if the simulation continues, the original coarse columnar grains would continue to grow, and the position of the crescent-shaped grains is inclined to generate new crescent-shaped grains rather than coarse columnar grains. The grains in **Figures 2(c)-(e)** consist of crescent-shaped grains and small strip-shaped grains, yet the coarse columnar grains no longer exist. The regular arrangement of these strip-shaped grains is basically consistent with **Figure 2(e)**. Inconsistent with **Figure 2(e)**, the number of strip-shaped grains distributed along the TD direction of each layer increases with speed, from 1 to 2 per period (**Figure 3(c)**), to 2 to 3 (**Figure 3(d)**), and finally 3 to 4 (**Figure 3(e)**).

In the BD-SD plane, strip-shaped grains extending through several layers to the top of the simulation area are shown in **Figure 3(a)**, which is the same with **Figure 2(a)**. The numbers of strip-shaped grains running through two or three layers of thickness are more than that in **Figure 2(a)**, because there are crescent-shaped grains in the BD-TD plane of **Figure 3(a)**. A lot of strip-shaped grains through two or three layers of thickness are shown in **Figure 3(b)** and their morphology is the dominant grain morphology of this plane. In **Figures 3(c)-(e)**, the strip-shaped grains with a length of one layer thickness are arranged in the BD-SD plane, that are the same with **Figure 2(e)**.

In the SD-TD plane, consistent with **Figure 2**, the results exhibit strip-shaped grains between the scanning paths. As shown in **Figure 3(a)**, the length of strip-shaped grains is nearly equal to the length of hatch without small round grains.

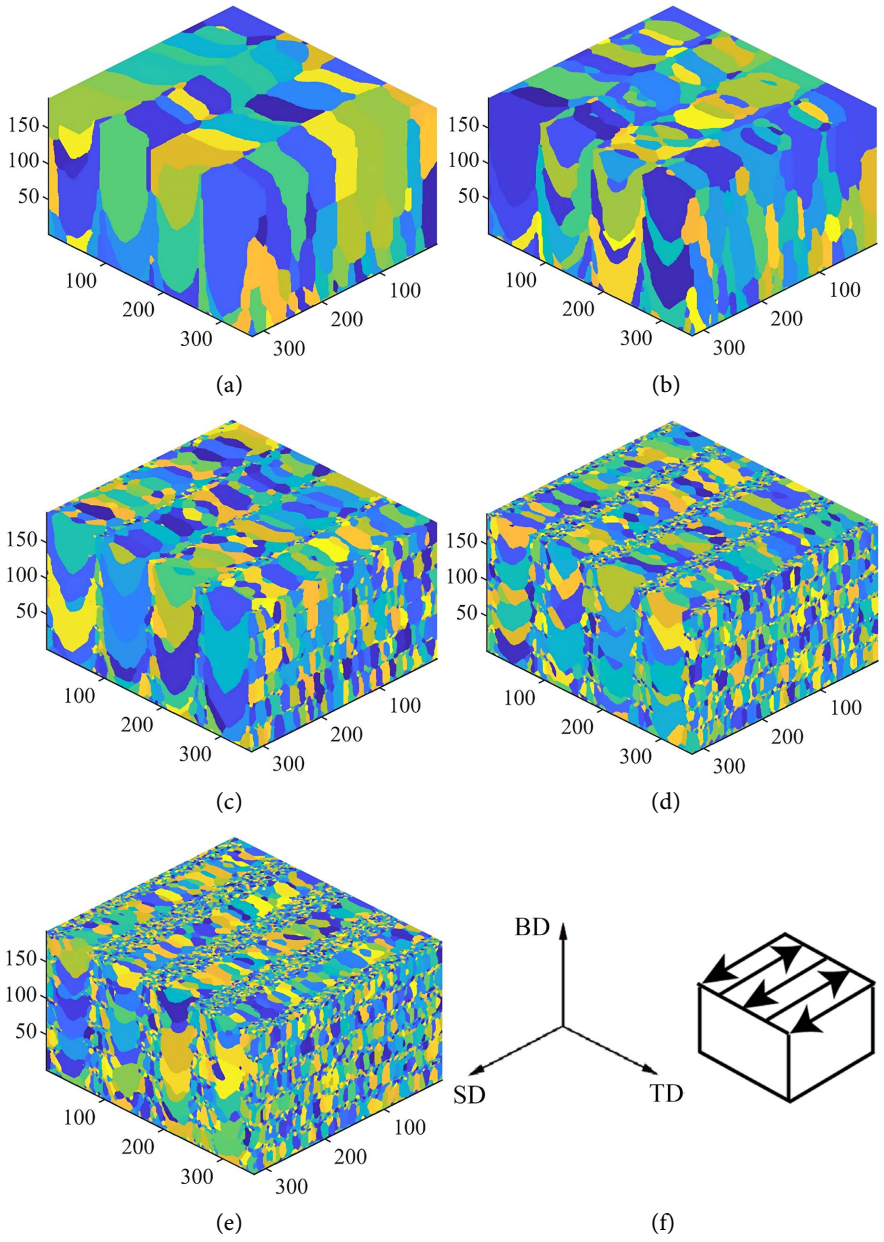

Figure 3. Simulation results of Group B. Five simulation results for five different scanning speeds, where (a) Speed = 13 site/MCS (b) Speed = 20 site/MCS (c) Speed = 27 site/MCS (d) Speed = 33 site/MCS (e) Speed = 40 site/MCS. (f) The coordinate system and scanning paths in the simulation results.

As small round grains begin to appear in the SD-TD plane, the length of strip-shaped grains is starting to shorten from Figure 3(b). The same with Figure 2, these small round grains are the top section of the grains observed in BD-TD plane. The small round grains observed in Figure 3(b) are the top section of the crescent-shaped grain tips in the BD-TD plane. The small round grains observed in Figures 3(c)-(e) are the top section of grains, including strip-shape grains and the tips of the crescent grains observed in the BD-TD plane. The small equiaxed grains with a size of only about 1-2 lattice sites are observed in Figure

3(d) and Figure 3(e). They are more numerous than in Figure 2(e).

Figure 4 exhibits the simulation results of Group C with the length ratio equal to 1 (μm/site = 1). The grain morphologies of 5 sets of speed are also different as shown in Figure 4. These simulation results are also different from Figure 2 and Figure 3.

In the BD-TD plane, the crescent-shaped grains through two or three layers are observed in Figure 3(a). Different from Figure 2(a) and Figure 3(a), the coarse columnar grains, which penetrating to the top of the simulation area, are

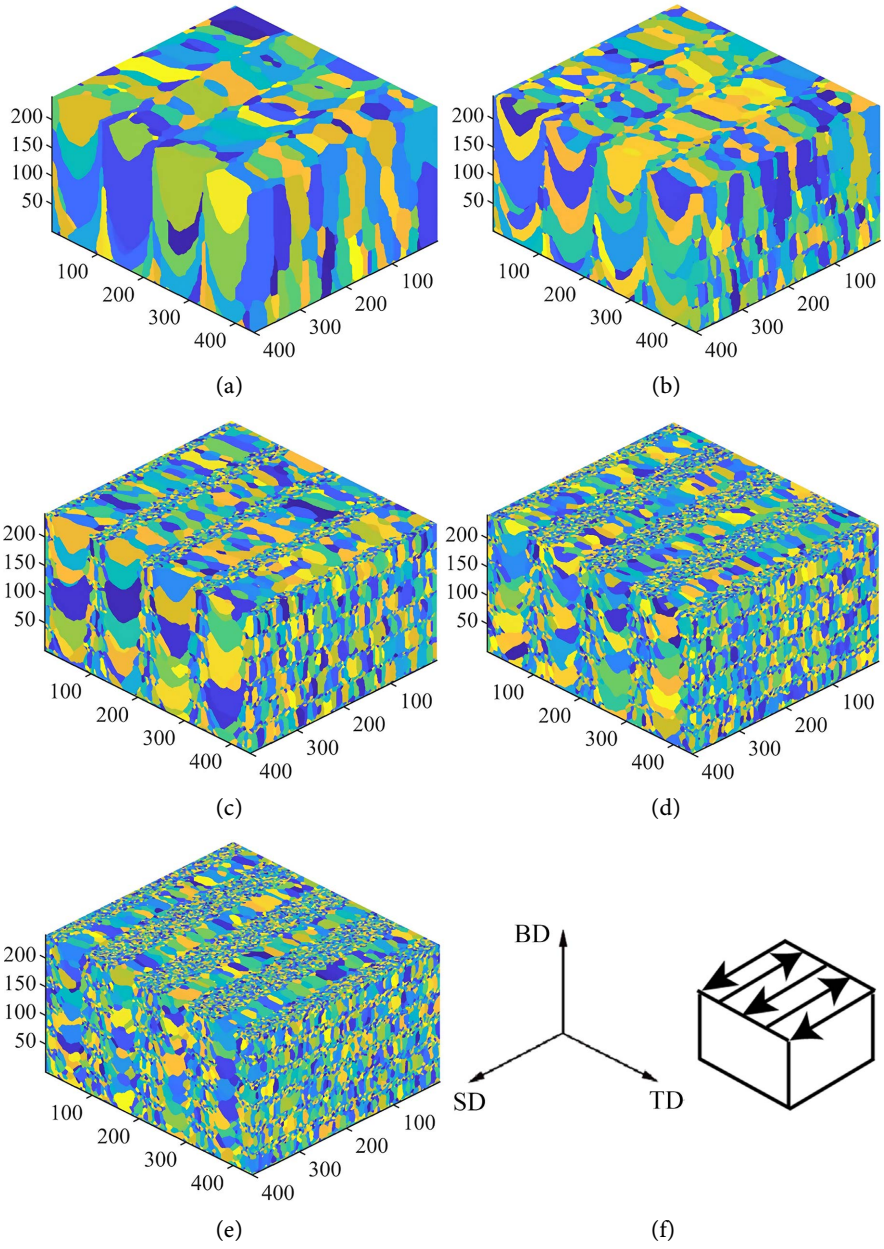

Figure 4. Simulation results of Group C. Five simulation results for five different scanning speeds, where (a) Speed =17 site/MCS (b) Speed = 25 site/MCS (c) Speed = 33 site/MCS (d) Speed = 42 site/MCS (e) Speed = 50 site/MCS. (f) The coordinate system and scanning paths in the simulation results.

no longer observed. Mixed grains consisting of crescent-shaped grains and periodically arranged strip-shaped grains start to appear in Figure 4(b). With the increase of the scanning speed, the crescent-shaped grains become smaller and smaller. The arrangement rule of strip-shaped grains is basically the same as that in Figure 2. However, the number of strip-shaped grains arranged in each period is different from that in Figure 2. As shown in Figure 4(b), approximately 1 or 2 strip-shaped grains are observed per period. In Figure 4(c), this number turns out to be 2 or 3 per period. In Figure 4(d), around 4 or 5 strip-shaped grains exist per period. Finally, generally 5 or 6 strip-shaped grains are presented in Figure 4(e). These different strip-shaped grains occupy the space of the original crescent grains, causing the crescent-shaped grains to become smaller.

In the BD-SD plane, strip-shaped grains through two or three layers of thickness are shown in Figure 4(a). There are no more strip-shaped grains extending through several layers to the top of the simulation area, such result is different from Figure 2(a). In Figure 4(b), strip-shaped grains through two or three layers of thickness and strip-shaped grains with a length of one layer thickness are observed meanwhile. In Figures 4(c)-(e), the main grains in Figure 4 are strip-shaped grains with a length of one layer thickness.

In the SD-TD plane, the strip-shaped grains between the scanning paths are presented in Figure 4. In Figure 4(a), the difference from Figure 2(a) is that strip-shaped grains and small round grains are observed at the same time. The small round grain is the top section of the tip of the crescent-shaped grain observed in the BD-TD plane. The small equiaxed grains with a size of only about 1 - 2 lattice sites and small round grains are observed in Figures 4(b)-(e). These small round grains consist of the top section of the tips of the crescent grains and strip-shape grains. The number of these small round grains and equiaxed grains increases with speed as shown in Figures 4(b)-(e).

3.2. Discussion

Since the scanning strategy of this work is parallel, the plane property perpendicular to the SD direction is similar, which means that BD-TD plane can reflect the properties of the whole simulation area. So, the following discussion is based on the results from BD-TD plane.

Qualitatively, two main types of grains emerge in the simulation results. One is the coarse columnar grains that run through several layers, and they grow to the top of the simulation area betweentimes. The other is the crescent-shaped grain. The two types of grains respectively presented at low and high scan speeds, which is in good agreement with the experimental results in the case of dynamic energy density respectively [6] [15]. Therefore, the simulation parameters of this work can be used as a reference to guide the matching of various simulation input parameters and experimental parameters.

In addition, as length ratio increases, the evolution trends of three simulation groups with the change of speed are similar. During this study, however, when the length ratio is getting larger and larger, the coarse columnar grains are dis-

appearing earlier and earlier, and the crescent-shaped grains are emerging sooner and sooner. That means the change in the length ratio results in a change in the ratio of unit physical time to unit simulation time.

In order to further explore the effect of the length ratio on the simulation results and better guide the matching of the simulation input parameters with the experimental parameters, the grain size of each simulation result was counted. The statistical results are shown in Figure 5. For better comparison, the results of the three sets of simulations were converted into physical lengths for comparison.

To reduce the error caused by the large number of small equiaxed grains with small area, the results in Figure 5 discard the data for the grains with the smallest area in the first 5%. In addition, ten sets of data from ten different BD-TD planes are used for each average grain size as a statistical dataset to reduce errors. It is reasonable because the BD-TD planar properties along the scanning direction are all similar.

As shown in Figure 5, the trends of the three group of outcome curves are similar. The simulation results of 3 groups take the maximum average grain size when the speed is 17 μm/MCS. However, the maximum average grain size of Group B is the same as the average grain size with scanning speed 27 μm/MCS in Group A. the maximum average grain size of Group C is the same as the average grain size with scanning speed 37 μm/MCS in Group A. This shows that as the ratio of unit physical length to unit simulation length increases, the ratio of unit physical time to unit simulation time decreases.

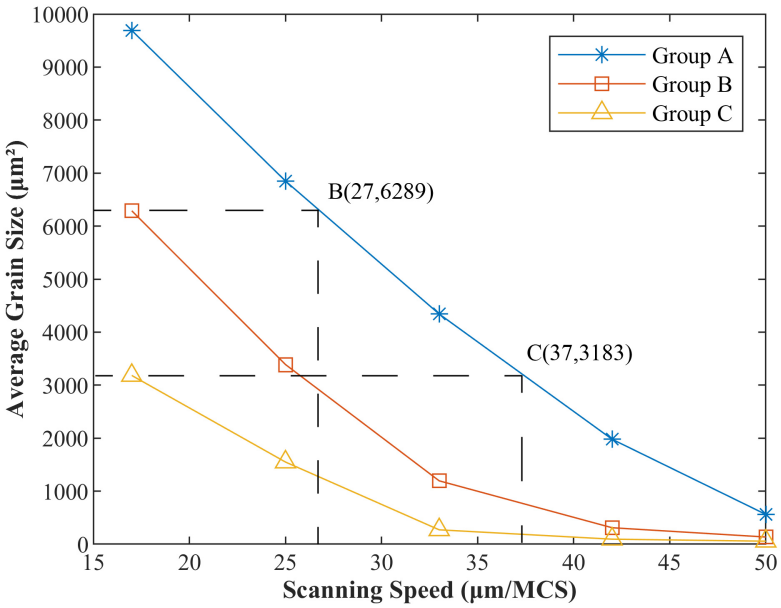

Figure 5. The relationship between grain size and scanning speed. The two points B and C are the intersection points of the two dotted line and curve of group A. These two dotted lines are parallel to the horizontal and pass through the highest points of the two curves of Group B and Group C, respectively. The 5 different physical speeds in the simulation are 17, 25, 33, 42, 50 μm/MCS (retain two significant figures).

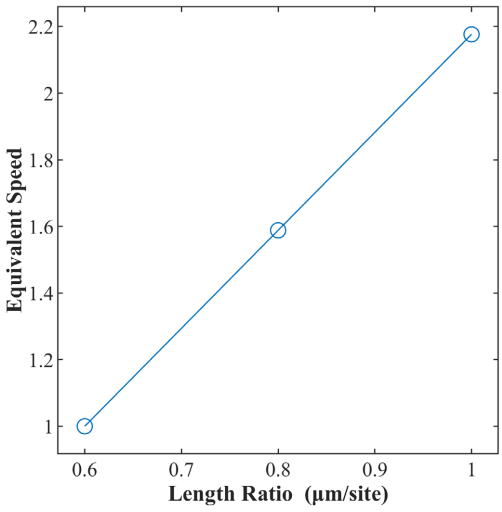

(a)

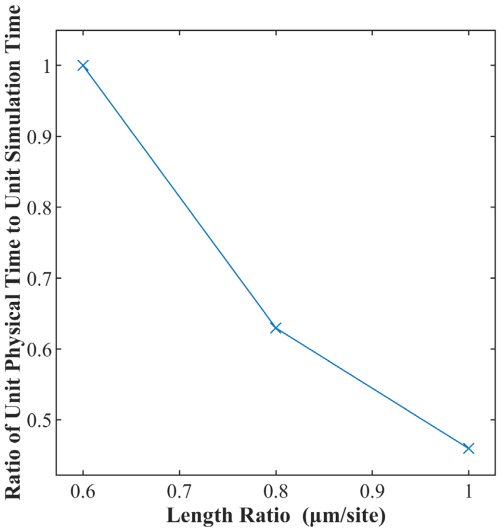

(b)

Figure 6. (a) The relationship between the length ratio and equivalent speed. The equivalent speed indicates the degree of change in the ratio of physical speed to simulation speed when the ratio of unit physical length to unit simulation length changes, with the results of group A as reference. (b) The relationship between length ratio and the ratio of unit physical time to unit simulation time. It reflects the change degree of the ratio of unit physical time to unit simulation time when the ratio of unit physical length to unit simulation length changes.

As shown in **Figure 6**, taking the simulation results of Group A as reference, discuss the change of velocity ratio and time ratio with the simulation length ratio. The equivalent speed and the ratio of unit physical time to unit simulation time are dimensionless. As the length ratio increases, the equivalent velocity increases approximately linearly and the ratio of unit physical time to unit simulation time gradually decreases. It should be noted that the ratio of unit physical time to unit simulation time in **Figure 6(b)** is the reciprocal of the equivalent velocity in **Figure 6(a)**.

4. Conclusions

In this work, the parallel scanning strategy of metal additive manufacturing is used for KMC simulation with 5 sets of different scanning speeds and 3 types of different length ratios as input parameters. The main conclusions are presented below:

1) With the increasing scanning speed, dominant grains in the simulation results changed from coarse columnar grains to crescent-shaped grains. This is consistent with the existing experimental results, and the parameters of this work can be used as a reference to fit the simulated input parameters and experimental parameters.

2) Changing the ratio of unit physical length to unit simulation length would have no significant effect on the trend of simulation results at different scanning speeds.

3) Variations in the ratio of unit physical length to unit simulation length will affect the ratio of unit physical time to unit simulation time in the simulation. As the length ratio increases, the ratio of unit physical time to unit simulation time gradually decreases.

Combined with the research content of this study, in the near future, establishing a database to match the input parameters of the KMC method with the experimental parameters of metal additive manufacturing of different processes and materials; exploring the evolution laws of the KMC method simulation under different $M(d)$ models, including the effect of the ratio of physical time to simulation, the evolution of grain morphology, will be interesting research directions.

Acknowledgements

The open-source KMC software mentioned above, SPPARKS can be downloaded at http://spparks.sandia.gov.

Conflicts of Interest

The authors declare no conflicts of interest regarding the publication of this paper.

References

[1] DebRoy, T., Mukherjee, T., Milewski, J.O., Elmer, J.W., Ribic, B., Blecher, J.J. and Zhang, W. (2019) Scientific, Technological and Economic Issues in Metal Printing and Their Solutions. *Nature Materials*, **18**, 1026-1032. https://doi.org/10.1038/s41563-019-0408-2

[2] American Society for Testing and Materials (2013) F2792-12a. Standard Terminology for Additive Manufacturing Technologies. ASTM International, West Conshohocken.

[3] DebRoy, T., Wei, H.L., Zuback, J.S., Mukherjee, T., Elmer, J.W., Milewski, J.O., *et al.* (2018) Additive Manufacturing of Metallic Components—Process, Structure and Properties. *Progress in Materials Science*, **92**, 112-224.

https://doi.org/10.1016/j.pmatsci.2017.10.001

[4] An, K., Yuan, L., Dial, L., Spinelli, I., Stoica, A.D. and Gao, Y. (2017) Neutron Residual Stress Measurement and Numerical Modeling in a Curved Thin-Walled Structure by Laser Powder Bed Fusion Additive Manufacturing. *Materials & Design*, **135**, 122-132. https://doi.org/10.1016/j.matdes.2017.09.018

[5] Nagase, T., Hori, T., Todai, M., Sun, S.H. and Nakano, T. (2019) Additive Manufacturing of Dense Components in Beta-Titanium Alloys with Crystallographic Texture from a Mixture of Pure Metallic Element Powders. *Materials & Design*, **173**, Article ID: 107771. https://doi.org/10.1016/j.matdes.2019.107771

[6] Ishimoto, T., Wu, S., Ito, Y., Sun, S.H., Amano, H. and Nakano, T. (2020) Crystallographic Orientation Control of 316L Austenitic Stainless Steel via Selective Laser Melting. *ISIJ International*, **60**, 1758-1764. https://doi.org/10.2355/isijinternational.ISIJINT-2019-744

[7] Tan, J.H. K., Sing, S.L. and Yeong, W.Y. (2020) Microstructure Modelling for Metallic Additive Manufacturing: A Review. *Virtual and Physical Prototyping*, **15**, 87-105. https://doi.org/10.1080/17452759.2019.1677345

[8] Körner, C., Markl, M. and Koepf, J.A. (2020) Modeling and Simulation of Microstructure Evolution for Additive Manufacturing of Metals: A Critical Review. *Metallurgical and Materials Transactions A*, **51**, 4970-4983. https://doi.org/10.1007/s11661-020-05946-3

[9] Gong, X. and Chou, K. (2015) Phase-Field Modeling of Microstructure Evolution in Electron Beam Additive Manufacturing. *JOM*, **67**, 1176-1182. https://doi.org/10.1007/s11837-015-1352-5

[10] Xiong, F., Huang, C., Kafka, O.L., Lian, Y., Yan, W., Chen, M. and Fang, D. (2021) Grain Growth Prediction in Selective Electron Beam Melting of Ti-6Al-4V with a Cellular Automaton Method. *Materials & Design*, **199**, Article ID: 109410. https://doi.org/10.1016/j.matdes.2020.109410

[11] Rodgers, T.M., Madison, J.D. and Tikare, V. (2017) Simulation of Metal Additive Manufacturing Microstructures Using Kinetic Monte Carlo. *Computational Materials Science*, **135**, 78-89. https://doi.org/10.1016/j.commatsci.2017.03.053

[12] Rodgers, T.M., Moser, D., Abdeljawad, F., Jackson, O.D. U., Carroll, J.D., Jared, B.H., *et al.* (2021) Simulation of Powder Bed Metal Additive Manufacturing Microstructures with Coupled Finite Difference-Monte Carlo Method. *Additive Manufacturing*, **41**, Article ID: 101953. https://doi.org/10.1016/j.addma.2021.101953

[13] Rodgers, T.M., Bishop, J.E. and Madison, J.D. (2018) Direct Numerical Simulation of Mechanical Response in Synthetic Additively Manufactured Microstructures. *Modelling and Simulation in Materials Science and Engineering*, **26**, Article ID: 055010. https://doi.org/10.1088/1361-651X/aac616

[14] Garcia, A.L., Tikare, V. and Holm, E.A. (2008) Three-Dimensional Simulation of Grain Growth in a Thermal Gradient with Non-Uniform Grain Boundary Mobility. *Scripta Materialia*, **59**, 661-664. https://doi.org/10.1016/j.scriptamat.2008.05.039

[15] Nadammal, N., Mishurova, T., Fritsch, T., Serrano-Munoz, I., Kromm, A., Haberland, C., *et al.* (2021) Critical Role of Scan Strategies on the Development of Microstructure, Texture, and Residual Stresses during Laser Powder Bed Fusion Additive Manufacturing. *Additive Manufacturing*, **38**, Article ID: 101792. https://doi.org/10.1016/j.addma.2020.101792